LETTERS
PUBLISHED ONLINE: 8 AUGUST 2010 | DOI: 10.1038/NMAT2822
nature materials

Designer spoof surface plasmon structures collimate terahertz laser beams

Nanfang Yu[1]*, Qi Jie Wang[1]†, Mikhail A. Kats[1], Jonathan A. Fan[1], Suraj P. Khanna[2], Lianhe Li[2], A. Giles Davies[2], Edmund H. Linfield[2] and Federico Capasso[1]*

Surface plasmons have found a broad range of applications in photonic devices at visible and near-infrared wavelengths. In contrast, longer-wavelength surface electromagnetic waves, known as Sommerfeld or Zenneck waves[1,2], are characterized by poor confinement to surfaces and are therefore difficult to control using conventional metallo-dielectric plasmonic structures. However, patterning the surface with subwavelength periodic features can markedly reduce the asymptotic surface plasmon frequency, leading to 'spoof' surface plasmons[3,4] with subwavelength confinement at infrared wavelengths and beyond, which mimic surface plasmons at much shorter wavelengths. We demonstrate that by directly sculpting designer spoof surface plasmon structures that tailor the dispersion of terahertz surface plasmon polaritons on the highly doped semiconductor facets of terahertz quantum cascade lasers, the performance of the lasers can be markedly enhanced. Using a simple one-dimensional grating design, the beam divergence of the lasers was reduced from ~180° to ~10°, the directivity was improved by over 10 decibels and the power collection efficiency was increased by a factor of about six compared with the original unpatterned devices. We achieve these improvements without compromising high-temperature performance of the lasers.

Metamaterials and transformation optics offer major opportunities for the control of electromagnetic fields[5–8]. The underlying paradigm is to design spatial variations of the magnitude and sign of the effective refractive index; thus, the optical path, or more generally the 'optical space', can be engineered in a continuous and almost arbitrary way. One can extend the concept to surface plasmon (SP) optics where the dispersion properties of SPs are tailored by nanostructuring metallic surfaces with designer patterns. In this context 'metasurfaces' or 'metafilms' have found interesting applications, such as subwavelength imaging[9], waveguiding[10,11] and the localization[10,11], confinement[12] and slowing of light[13].

Consider a structure composed of arrays of grooves with subwavelength periodicities textured on the surface of a plasmonic material (metals or highly doped semiconductors, which behave as metals in the terahertz regime; see Fig. 1a). Such a structure supports strongly confined surface waves with a dispersion relation $\omega(\beta)$ similar to SPs on a planar metal surface in the visible regime, as calculated by Pendry, Martín-Moreno, and García-Vidal[3,4] and observed on structured metals at terahertz frequencies[14]. The asymptotic frequency, ω_{spoof}, is not solely determined by properties of the interface materials and can be designed over an extremely wide range by engineering the subwavelength pattern on the interface[3]. If the metal can be treated as a perfect electric conductor, $\omega_{spoof} = \pi c/2h$, where h is the groove depth and c is the speed of light in vacuum[4]. Physically, this corresponds to first-order standing waves along the depth of the grooves. As ω_{spoof} is primarily determined by surface texturing, one can engineer the spoof SP dispersion curve and obtain a sizeable deviation between the curve and the light line at terahertz frequencies; that is, $\beta(\omega_{THz}) > k_o(\omega_{THz})$ (refs 3,4,14; see Fig. 1b). Here β is the in-plane wave vector of the SPs and k_o is the free-space wave vector. As a result, the out-of-plane wave vector $\kappa(\omega_{THz}) = i\sqrt{\beta^2(\omega_{THz}) - k_0^2(\omega_{THz})}$ can be considerable, corresponding to confined SPs with a 1/e decay distance in the air normal to the interface equal to $1/|\kappa|$ (ref. 14).

In this Letter, we demonstrate the great design potential of spoof SP structures for active photonic devices by markedly improving the performance of terahertz quantum cascade lasers (QCLs). Terahertz QCLs have undergone rapid development recently and have significant potential for applications in sensing, imaging and heterodyne detection of chemicals[15–18]. Terahertz QCLs with the highest operating temperature and lowest threshold current so far take advantage of the high optical confinement (near 100%) and heat removal properties of a double-metal waveguide design, in which the laser active region is located between a metal strip and a metal plane[19–21]. However, this leads to non-Fresnel reflection at the subwavelength laser apertures (as small as one-tenth of λ_o, the free-space wavelength), which gives rise to inefficient power out-coupling (power reflectivity of laser modes at the aperture up to 90%) and poor beam quality (characterized by a divergence angle ~180° perpendicular to the laser material layers)[20,21]. The last of these is a particularly serious problem for the far-infrared heterodyne detection of chemicals because the output of terahertz QCLs (local oscillator) must be focused into a small-area Schottky diode mixer[15].

A number of schemes have been demonstrated to increase beam directionality and/or power out-coupling efficiency of terahertz QCLs (refs 22–27). One approach is to attach a silicon microlens[22] or a metallic horn antenna[23] onto one of the facets of the laser waveguide to reduce the mode impedance mismatch at the laser aperture, and thereby enhance the power output. However, this method requires meticulous manipulation and alignment of small optical components, which affects device yield and robustness. A monolithic approach would alleviate these problems. Another approach relies on processing terahertz lasers into surface-emitting structures with higher-order gratings[24–26] or photonic crystals[27]; this approach relies on constructive interference between multiple surface emissions or a large emission area to reduce beam divergence. However, this results in devices with reduced mode confinement and therefore increases the laser threshold current

[1]School of Engineering and Applied Sciences, Harvard University, Cambridge, Massachusetts 02138, USA, [2]School of Electronic and Electrical Engineering, University of Leeds, Leeds LS2 9JT, UK. †Present address: School of Electrical and Electronic Engineering & School of Physical and Mathematical Sciences, Nanyang Technological University, 50 Nanyang Avenue, Singapore 639798, Singapore. *e-mail: nyu@fas.harvard.edu; capasso@seas.harvard.edu.

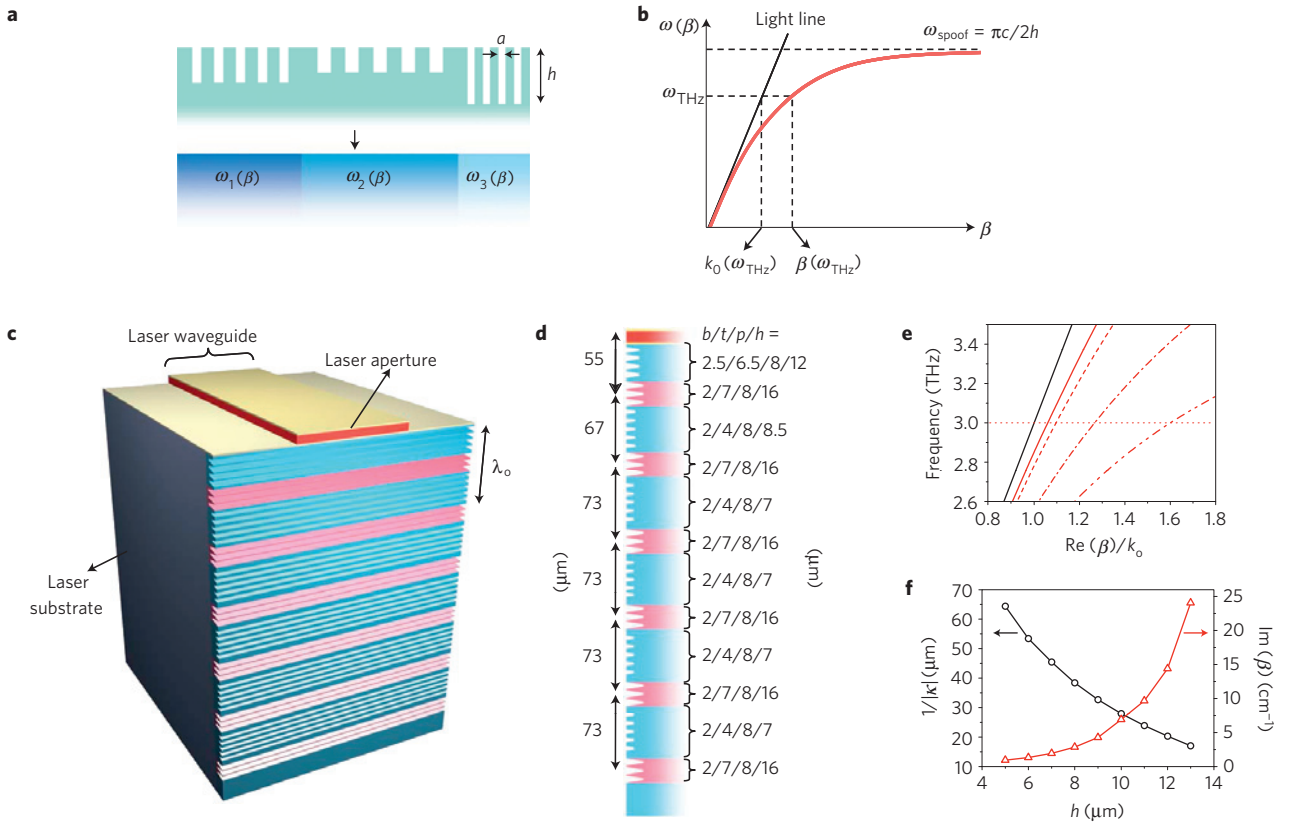

Figure 1 | Terahertz plasmonic collimator design. a, By texturing a metal or a metallic semiconductor surface with subwavelength structures of various geometries, one can engineer the dispersion of SPs. In this way, complex designer plasmonic structures can be constructed to greatly improve device performance or to realize new functionalities. **b**, Schematic dispersion curve for terahertz spoof SPs on a perfect metal. The asymptote of the curve, ω_{spoof}, the in-plane wave vector, β, and the out-of-plane wave vector, $\kappa = i\sqrt{\beta^2 - k_0^2}$, can be tailored by changing the geometry of the subwavelength grooves. **c**, Schematic of a terahertz QCL patterned with a spoof SP collimator. The plasmonic patterns are directly sculpted on the highly doped GaAs facet of the device. Artificial colouring in the figure indicates deep and shallow spoof SP grooves. The 'blue' grooves adjacent to the laser aperture increase device power throughput by coupling more laser output into spoof SPs on the facet; the deep 'pink' grooves modulate the dispersion properties of SPs on the facet, creating a second-order grating for power out-coupling; the shallow 'blue' grooves contribute to SP confinement. **d**, Cross-section of the design for a $\lambda_o = 100\,\mu m$ device. All of the grooves have trapezoidal cross-sections to resemble structures fabricated by FIB milling. The bottom and top of the grooves, their period and depth are labelled as *b*, *t*, *p* and *h*, respectively. **e**, The black curve is the dispersion diagram of surface waves on the planar semiconductor/air interface. In this frequency range, it is essentially linear with a slope extremely close to the speed of light in vacuum, a manifestation of the poor confinement of surface waves at terahertz frequencies. The red curves are the dispersion diagrams corresponding to the different sections of the collimator. Red solid curve: $b/t/p/h = 2/4/8/7\,\mu m$; red dashed curve: $b/t/p/h = 2/4/8/8.5\,\mu m$; red dash-dotted curve: $b/t/p/h = 2.5/6.5/8/12\,\mu m$; red dash-double-dotted curve: $b/t/p/h = 2/7/8/16\,\mu m$. The horizontal dotted line indicates the lasing frequency. $k_o = 2\pi/\lambda_o$, where $\lambda_o = 100\,\mu m$. **f**, Black open circles: the 1/*e* decay length of the spoof SP electric field ($|E|$) normal to the interface into the air as a function of *h*. Red open triangles: imaginary part of the in-plane wave vector as a function of *h*, which characterizes propagation loss of spoof SPs. Other groove dimensions are fixed: $b/t/p = 2/4/8\,\mu m$.

density, which usually leads to reduced maximum operating temperatures in continuous-wave operation.

Conventional metallo-dielectric plasmonic structures defined on laser facets have been used to shape the wavefront of mid-infrared semiconductor lasers[28–31]. Unfortunately this methodology is not scalable to far-infrared wavelengths, because those structures do not significantly modify the SP dispersion properties and in particular the asymptotic SP frequency, thus providing limited control of terahertz surface waves.

A schematic of our design for a 3 THz frequency ($\lambda_o = 100\,\mu m$) laser and its cross-section are shown in Fig. 1c and d, respectively. The double-metal waveguide of the laser is defined on a 450-μm-thick highly doped GaAs substrate. Two colours are used in Fig. 1c,d to identify shallow and deep spoof SP grooves. All of the grooves are defined directly on the GaAs substrate without any metal coating. We take advantage of the fact that in the terahertz regime the carrier concentration in highly doped semiconductors is sufficiently large that the semiconductor is 'metallic' with the real part of its dielectric permittivity being largely negative (see the Methods section for more details).

At the aperture of the double-metal waveguide, the laser emits both directly into the far-field and also into surface waves on the device facet. In the original unpatterned device, both components have a wave vector close to k_o. The wave vector of the laser mode in the waveguide is several times larger, $\sim n_{eff} k_o$ ($n_{eff} \approx 3.5$ is the effective mode index). Therefore, there is a wave vector mismatch of the modes at the aperture. In our collimator, the spoof SP grooves adjacent to the aperture increase the effective in-plane wave vector of the SPs, reducing the wave vector mismatch. More light is therefore coupled out from the laser cavity and a larger percentage of it is channelled into the spoof SP modes instead of being directly emitted into the far-field. In addition, the deep grooves (pink in Fig. 1d) periodically modulate the dispersion of the SPs on the device facet, creating an effective second-order grating that scatters the energy of the SPs into the far-field. Constructive interference between these scattered waves and the direct emission

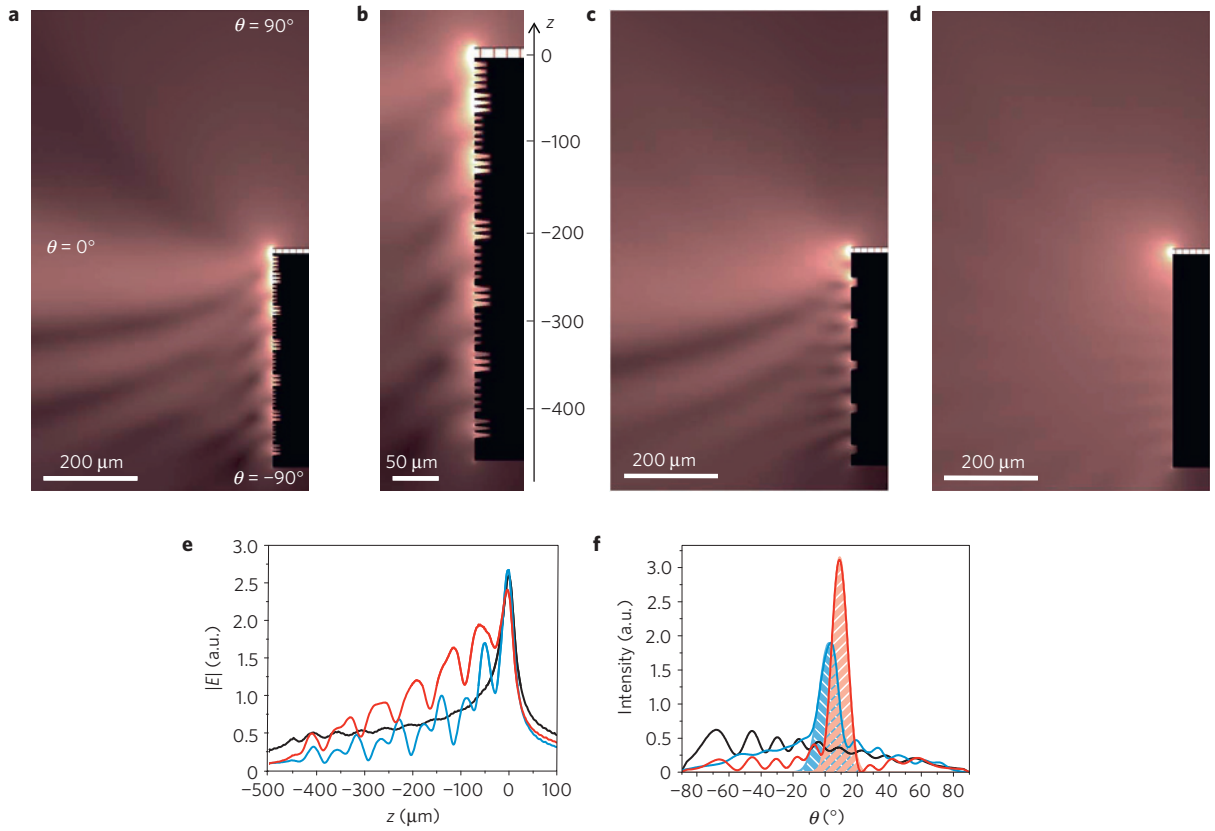

Figure 2 | Simulations. a, Simulated distribution of the electric field ($|E|$) of the device shown in Fig. 1. The simulation plane is perpendicular to the laser facet and along the plane of symmetry of the laser waveguide. **b**, Zoom-in view of **a** showing the region around the device facet. **c**,**d**, Simulated electric-field distribution ($|E|$) of a device with a conventional second-order grating (**c**) and of the original device (**d**). The conventional second-order grating was optimized to give the highest directivity, although it is still less effective than the spoof SP collimator. The centre-to-centre distance between the aperture and the closest groove of the second-order grating is 65 μm. The grating period is 88 μm. The opening, bottom and depth of the second-order grating grooves are 19, 15 and 13.5 μm, respectively. **e**, The red, blue and black curves are line-scans of the near-field ($|E|$) along and 10 μm above the facet for the devices in **a**, **c** and **d**, respectively. **f**, The red, blue and black curves are calculated vertical far-field intensity profiles ($|E|^2$) for **a**, **c** and **d**, respectively. Gaussian fits to the central lobes of the blue and red curves are plotted and the area under the fits is shaded light blue and light red, respectively. The shaded area is a measure of the percentage of total optical power in the main lobe. The main lobe of the device with the terahertz spoof SP collimator contains 70% of the output power, whereas it contains only 45% for the device with the second-order grating.

from the laser aperture gives rise to a low-divergence beam normal to the facet in the far-field[28,29]. Most importantly, the shallow grooves (blue in Fig. 1d) greatly increase the confinement of SPs, thus improving the scattering efficiency of the second-order grating. We use the concept of directivity D, borrowed from antenna theory, to characterize collimation for our devices. Directivity is defined as $D = 10\log_{10}(2\pi I_{\mathrm{peak}}/I_{\mathrm{total}})$ (ref. 32), where I_{peak} is the far-field peak intensity and I_{total} is the total intensity under the beam profile. In summary, the spoof SP structures are multifunctional; by engineering the dispersion of SPs, they form a collimator that improves device power throughput and increases directivity.

To better understand the effect of the spoof SP grooves, we calculated the dispersion curves, the confinement and propagation losses of spoof SPs for different groove geometries (Fig. 1e,f). The in-plane wave vector increases by ~25% for the grooves adjacent to the laser aperture (red dash–dotted curve in Fig. 1e), which reduces mode impedance mismatch, thus increasing optical power throughput owing to improved coupling into spoof SP modes, as discussed previously. The depth of the shallow grooves (blue in Fig. 1d) was chosen to be in the range 7–12 μm to provide sufficient confinement without introducing large optical losses, which are mainly due to ohmic absorption and rise sharply as the groove depth increases[33]. Figure 1f shows that the confinement of SPs is improved to a few tens of micrometres, representing a reduction by approximately one order of magnitude compared with Zenneck waves on a planar interface (~300 μm). The depth of the shallow grooves (blue in Fig. 1d) decreases away from the laser aperture to reduce absorption losses. This leads to a non-constant SP phase velocity, which is smaller in the regions closer to the aperture. To make sure that all of the scattered waves are in phase to maximize constructive interference, the periods of the second-order grating are chosen to be shorter in the vicinity of the aperture.

The simulated electric-field distribution of the device is presented in Fig. 2a. Waves scattered from the laser facet by the spoof SP collimator are clearly observed in the near- and meso-field, and on closer inspection (Fig. 2b), confined spoof SPs can be seen on the facet. As a comparison, the simulated electric-field distributions for a device with a conventional second-order grating and for the original device without any facet patterning are presented in Fig. 2c and d, respectively. Figure 2e shows line-scans of the near-fields of three devices. Note that the near-fields on the facet are the strongest for the device with the spoof SP collimator. This is due to the improved confinement of SPs, as well as the increased device power throughput and a more efficient coupling into the spoof SP modes. Indeed, simulations indicate that compared with the original unpatterned device, the power throughput of the device with the spoof SP collimator is increased by approximately 25%. On the basis of the simulation results in

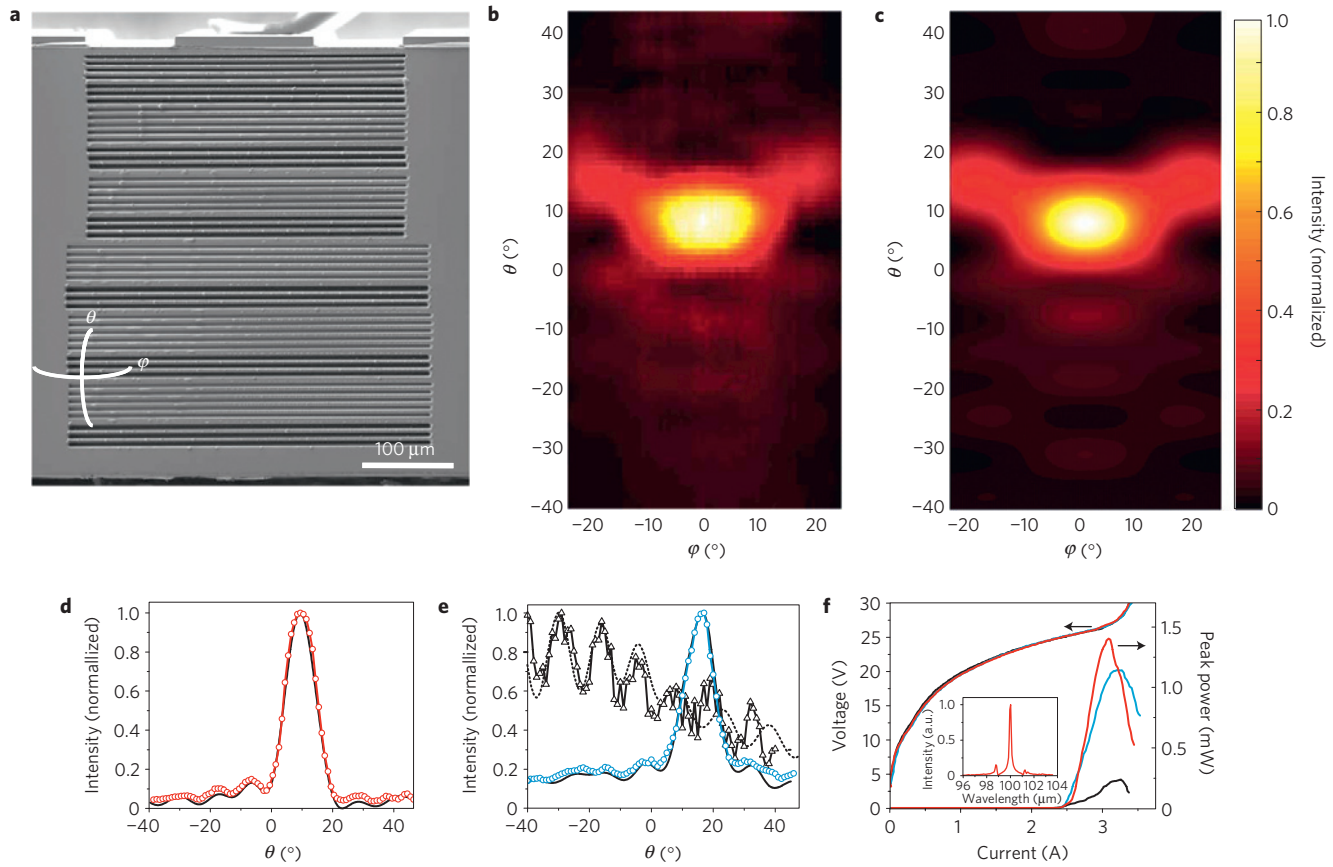

Figure 3 | Experimental results for a device fabricated according to the design in Fig. 1. a, Scanning electron microscope image of the device facet. The device has a 1.2-mm-long, 150-μm-wide and 10-μm-thick waveguide and lases at $\lambda_o = 100$ μm. The plasmonic pattern is wider at the bottom part to further expand the wavefront of SPs. **b**,**c**, Measured (**b**) and simulated (**c**) 2D far-field intensity profiles of the device. **d**, Line-scans of **b** (red circles) and **c** (black curve) along $\varphi = 0°$. The far-field measurement range is from $\theta = -40°$ to $\theta = +45°$ in the vertical direction, limited by the window of the cryostat. **e**, The black triangles and black dotted curve are, respectively, measured and simulated laser intensity profiles along $\varphi = 0°$ for the original unpatterned device. The blue circles and black solid curve are, respectively, measured and simulated laser intensity profiles along $\varphi = 0°$ for the device after defining the second-order grating (pink in Fig. 1d). **f**, Power output and voltage as a function of pump current for the device. The black, blue and red curves are for the unpatterned device, the device with only the second-order grating and the device with the spoof SP collimator, respectively. Inset: Spectrum of the device with the spoof SP collimator measured at $I = 3.0$ A. The 2D far-field map shown in **b** was taken at this current. The spectrum shows one comb of longitudinal modes belonging to the fundamental TM_{00} transverse mode of the waveguide.

Fig. 2a, it is estimated that 45% of the laser output is coupled into the spoof SP modes on the facet and the remaining 55% is emitted directly into the far-field. In contrast, the simulation with only the second-order grating (Fig. 2c) shows that the power coupled into surface waves is merely 15%, and the remaining 85% is radiated directly into the far-field. As a result of a more uniform intensity distribution in the near-field, the device with the spoof SP collimator shows increased directivity, from ~10 dB for the device with the second-order grating to ~16 dB (see Fig. 2f).

The experimental realization of the collimator is shown in Fig. 3. Figure 3a is a scanning electron microscope image of the facet of a device fabricated using focused ion beam (FIB) milling according to the design in Fig. 1d. The collimator occupies a small footprint with dimensions $\sim 4\lambda_o \times 4.5\lambda_o$. The measured two-dimensional (2D) far-field intensity profile of the device and its vertical line-scan are presented in Fig. 3b and d, respectively. The central beam has vertical and lateral divergence angles of ~11.7° and ~16°, respectively (full-width at half-maximum); the optical background has an average intensity that is below 10% of the central lobe peak intensity. Both are in good agreement with the 3D full-wave simulation results in Fig. 3c,d. The emission of the original device is highly divergent (see Fig. 3e for its vertical far-field profile). The measured beam directivity is increased from ~5 dB for the original unpatterned laser, to ~11 dB for the device with only the second-order grating (pink in Fig. 1d) and to ~16 dB for the device with the spoof SP collimator, representing a major performance improvement. The directivity of our collimated device is better than or comparable to those obtained in terahertz QCLs with higher-order gratings, photonic crystals or mounted micro optical elements[22–27]. The small-divergence beam emitted from our terahertz device is compatible with the receiver front end of modern submillimetre heterodyne detection systems[34,35].

Reduction of beam divergence occurs in both the vertical and lateral directions. In the vertical direction, the collimation is essentially an antenna array effect[28,29,31]. In the lateral direction, it is due to an increased emission area: the spoof SP patterns were intentionally chosen to be wider than the laser waveguide (Fig. 3a), which helps spread SPs laterally by using a transmission line effect (see Supplementary Information for more details). As such, 2D collimation was realized using a 1D structure composed of straight grooves; this is different from ring-shaped 2D plasmonic collimators for mid-infrared QCLs (ref. 28).

The collected power of the device with the terahertz spoof SP collimator increases by a factor of ~6 compared with the original unpatterned device under the same measurement conditions (see Fig. 3f). The enhancement factor is ~5 for the device with

only the second-order grating (pink in Fig. 1d). This difference in measured power is primarily a result of the increased total power throughput originating from the reduced wave vector mismatch in the spoof SP collimator. Our power measurement apparatus with a collection cone of ∼50° captures the main lobe as well as a significant portion of the background light. Eventually, what matters most for applications is the power carried in the main lobe of a laser beam, because the optical background outside the main lobe is often lost during propagation in optical systems. On the basis of the far-field measurements, the power in the main lobe of the device with the spoof SP collimator is about two times larger than that of the device with only the second-order grating.

The maximum operating temperature of the patterned device is 135 K, the same as that of the original device. Figure 3f shows that the lasing threshold was not changed after defining the collimator. The threshold is proportional to the sum of waveguide loss, α_w, mainly resulting from absorption in the waveguide material, and mirror loss, α_m, resulting from out-coupling of laser light from the facets. In our devices, α_w is about 30 times larger than α_m, so even a significant increase in α_m will not lead to a noticeable increase of the threshold.

The ability to confine low-frequency surface waves to subwavelength scales can lead to their more efficient manipulation and stronger interaction with analytes on the surface; the capability to engineer at will the dispersion properties of SPs may facilitate optical impedance matching between different components in an optical system. Furthermore, we plan to build devices with reconfigurable functions by using doped semiconductors as the plasmonic media, because their optical properties (for example, permittivity, anisotropy) can be tuned by applying optical excitation, electrical potentials or magnetic fields, or by controlling the temperature. We believe that these functionalities will lead to developments in plasmonics and metamaterials where key problems in imaging, sensing, wavefront engineering, slow light and photovoltaics will be addressed.

Methods

Devices and fabrication. The QCL material was grown by molecular beam epitaxy on an undoped GaAs substrate. The growth sequence started with a 250-nm-thick undoped GaAs buffer layer, and was followed by a 300-nm-thick $Al_{0.5}Ga_{0.5}As$ etch-stop layer, a 75-nm-thick layer of GaAs n-doped to 5×10^{18} cm^{-3}, the active region and finally a 50-nm-thick GaAs layer n-doped to 5×10^{18} cm^{-3}. The active region consists of 170 periods of a two-phonon-resonance active region design similar to that of ref. 36, with a doping sheet density of $n_s = 3.65 \times 10^{10}$ cm^{-2}. The material was processed into copper–copper waveguides using the following procedure[19]. First, a square centimetre of QCL material was cleaved and sputter-coated with Ta/Cu/Au (15/500/500 nm). The material was then wafer-bonded to a highly doped (1.6×10^{18} cm^{-3}) GaAs substrate coated with sputtered layers of Ti/Au (15/500 nm). The bonded QCL wafer was next polished and wet-etched down to the etch-stop layer with a hydrogen peroxide/ammonium hydroxide solution (19:1 in volume), and the etch-stop layer was stripped with concentrated hydrofluoric acid. The laser ridges, with widths ranging from 25 to 150 μm, were then defined using dry etching with an SU-8 2005 photoresist mask. After SU-8 removal, metal (Ta/Cu/Au, 15/100/30 nm) was sputtered on top of the laser ridges. A gold capping layer was added to the waveguides with copper cladding to avoid copper oxidation and to facilitate wire bonding. The processed wafers were finally cleaved into 1–2-mm-long bars and indium-mounted onto copper blocks.

The back facets of QCLs were coated with 300-nm Al_2O_3 and 100-nm gold so that the measured far-field profiles are solely due to emission from the front facets. We note that in devices without back-facet coating and front-facet patterning, the highly divergent emissions from the front and the back apertures interfere with each other, which gives rise to unpredictable far-field patterns that depend sensitively on the geometries of the laser ridges[37,38]. To suppress higher-order transverse modes in our wide-ridge devices, side-absorbers[39] were defined by removing ∼3–4-μm-wide strips of metal along the edges of the device top contact. Devices fabricated in this way have maximum operating temperatures ∼10°–20° lower compared with devices without side-absorbers.

The plasmonic patterns were sculpted into the semiconductor substrate using FIB milling (Zeiss NVision 40) at a high ion current of 13 or 27 nA to limit fabrication time. The diameter of the Ga ion beam at this current is ∼1 μm, which gives rise to a trapezoidal cross-section of the fabricated grooves.

Optical constants. The highly doped semiconductor substrate supports surface waves in the terahertz spectral range. We used the Drude model to calculate the dielectric permittivity of highly doped GaAs at terahertz frequencies[40,41] and found that the real part of the permittivity is negative. For example, $\varepsilon_{GaAs} \sim -200 + 42i$ for our device and measurement conditions ($\lambda_o = 100$ μm, GaAs n-doped to 1.6×10^{18} cm^{-3}, $T = 80$ K). The propagation distance of surface waves (defined as the 1/e decay length of the electric field) along a planar GaAs/air interface under these conditions corresponds to ∼3 cm (∼300λ_o), which is about 10% of that of surface waves on a planar gold surface. Therefore, the highly doped GaAs functions like a poor metal at terahertz frequencies, which is unlike the situation for visible and near-infrared wavelengths. It is extremely beneficial that metals are not needed for plasmonics in the terahertz regime, because this greatly simplifies device fabrication.

In our system (surface-corrugated GaAs n-doped to 1.6×10^{18} cm^{-3} at $T = 80$ K), the determination of the asymptotic frequency of the spoof SP dispersion curve is quite complicated because it involves three factors: the subwavelength pattern, the free-carrier concentration and the restrahlen band of GaAs. If one assumes that the spoof SP pattern is defined in a perfect electric conductor, the asymptotic frequency will ∼30–67 THz for the groove geometries used. However, it will be further lowered considering the actual dielectric permittivity of GaAs, which is affected by the free-carrier concentration and the restrahlen band of GaAs. On one hand, the Drude model predicts that the free-carrier concentration is able to support 'metallic' GaAs (that is, the real part of the permittivity <0) up to ∼10 THz. On the other hand, the restrahlen band of GaAs (∼7.5–10 THz; ref. 42) is going to introduce a large negative permittivity when an electromagnetic field strongly interacts with the optical phonons. The actual asymptotic frequency is therefore ∼7.5 THz primarily determined by the restrahlen band of GaAs.

Measurements. All devices were tested in pulsed mode with 60-ns pulses at 0.3% duty cycle (60-ns pulses at a 100 kHz repetition rate, with an extra 1 kHz modulation at 50% duty cycle for lock-in detection). Laser powers were measured using a Fourier transform infrared (FTIR) spectrometer with a calibrated helium-cooled bolometer using two 2″-diameter parabolic mirrors: one with a 5 cm focal length to pass light from the devices to the input of the FTIR spectrometer, and the other with a 15 cm focal length to focus the light from the output of the FTIR spectrometer onto the bolometer. To map the 2D far-field emission profile of the devices, a cryostat, in which the lasers were mounted vertically (laser material layers normal to the horizontal plane), was placed on a rotation stage. Line-scans of the laser far-field along the θ direction were obtained as the stage was rotated in the horizontal plane. The relative height of the cryostat and the bolometer was adjusted to allow many line-scans of the device far-field to be obtained, and finally constructed into a 2D map.

Received 10 March 2010; accepted 30 June 2010; published online 8 August 2010

References

1. Zenneck, J. Über die Fortpflanzung ebener elektromagnetischer Wellen längs einer ebenen Leiterfläche und ihre Beziehung zur drahtlosen Telegraphie. *Ann. Phys.* **23,** 846–866 (1907).
2. Sommerfeld, A. Über die Ausbreitung der Wellen in der drahtlosen Telegraphie. *Ann. Physik* **28,** 665–736 (1909).
3. Pendry, J. B., Martín-Moreno, L. & García-Vidal, F. J. Mimicking surface plasmons with structured surfaces. *Science* **305,** 847–848 (2004).
4. García-Vidal, F. J., Martín-Moreno, L. & Pendry, J. B. Surfaces with holes in them: New plasmonic metamaterials. *J. Opt. A: Pure Appl. Opt.* **7,** S97–S101 (2005).
5. Engheta, N. & Ziolkowski, R. W. *Metamaterials: Physics and Engineering Explorations* (Wiley-IEEE Press, 2006).
6. Cai, W. & Shalaev, V. M. *Optical Metamaterials: Fundamentals and Applications* (Springer, 2009).
7. Pendry, J. B., Schurig, D. & Smith, D. R. Controlling electromagnetic fields. *Science* **312,** 1780–1782 (2006).
8. Leonhardt, U. Optical conformal mapping. *Science* **312,** 1777–1780 (2006).
9. Smolyaninov, I. I., Hung, Y-J. & Davis, C. C. Imaging and focusing properties of plasmonic metamaterial devices. *Phys. Rev. B* **76,** 205424 (2007).
10. Beermann, J., Radko, I. P., Boltasseva, A. & Bozhevolnyi, S. I. Localized field enhancements in fractal shaped periodic metal nanostructures. *Opt. Express* **15,** 15234–15241 (2007).
11. Radko, I. P. *et al.* Plasmonic metasurfaces for waveguiding and field enhancement. *Laser Photon. Rev.* **3,** 575–590 (2009).
12. Navarro-Cía, M. *et al.* Broadband spoof plasmons and subwavelength electromagnetic energy confinement on ultrathin metafilms. *Opt. Express* **17,** 18184–18195 (2009).
13. Gan, Q., Fu, Z., Ding, Y. J. & Bartoli, F. J. Ultrawide-bandwidth slow-light system based on THz plasmonic graded metallic grating structures. *Phys. Rev. Lett.* **100,** 256803 (2008).
14. Williams, C. R. *et al.* Highly confined guiding of terahertz surface plasmon polaritons on structured metal surfaces. *Nature Photon.* **2,** 175–179 (2008).

15. Hajenius, M. *et al.* Surface plasmon quantum cascade lasers as terahertz local oscillators. *Opt. Lett.* **33,** 312–314 (2008).
16. Kim, S. M. *et al.* Biomedical terahertz imaging with a quantum cascade laser. *Appl. Phys. Lett.* **88,** 153903 (2006).
17. Lee, A. W. M. *et al.* Real-time terahertz imaging over a standoff distance (>25 meters). *Appl. Phys. Lett.* **89,** 141125 (2006).
18. Hübers, H-W. *et al.* High-resolution gas phase spectroscopy with a distributed feedback terahertz quantum cascade laser. *Appl. Phys. Lett.* **89,** 061115 (2006).
19. Belkin, M. A. *et al.* High-temperature operation of terahertz quantum cascade laser sources. *IEEE J. Sel. Top. Quantum Electron.* **15,** 952–967 (2009).
20. Williams, B. S. Terahertz quantum-cascade lasers. *Nature Photon.* **1,** 517–525 (2007).
21. Scalari, G. *et al.* THz and sub-THz quantum cascade lasers. *Laser Photon. Rev.* **3,** 45–66 (2009).
22. Lee, A. W. M. *et al.* High-power and high-temperature THz quantum-cascade lasers based on lens-coupled metal–metal waveguides. *Opt. Lett.* **32,** 2840–2842 (2007).
23. Amanti, M. I., Fischer, M., Walther, C., Scalari, G. & Faist, J. Horn antennas for terahertz quantum cascade lasers. *Electron. Lett.* **43,** 573–574 (2007).
24. Fan, J. A. *et al.* Surface emitting terahertz quantum cascade laser with a double-metal waveguide. *Opt. Express* **14,** 11672–11680 (2006).
25. Mahler, L. *et al.* Vertically emitting microdisk lasers. *Nature Photon.* **3,** 46–49 (2009).
26. Amanti, M. I., Fischer, M., Scalari, G., Beck, M. & Faist, J. Low-divergence single-mode terahertz quantum cascade laser. *Nature Photon.* **3,** 586–590 (2009).
27. Chassagneux, Y. *et al.* Electrically pumped photonic-crystal terahertz lasers controlled by boundary conditions. *Nature* **457,** 174–178 (2009).
28. Yu, N. *et al.* Plasmonics for laser beam shaping. *IEEE Trans. Nanotech.* **9,** 11–29 (2010).
29. Yu, N. *et al.* Small-divergence semiconductor lasers by plasmonic collimation. *Nature Photon.* **2,** 564–570 (2008).
30. Yu, N. *et al.* Semiconductor lasers with integrated plasmonic polarizers. *Appl. Phys. Lett.* **94,** 151101 (2009).
31. Yu, N. *et al.* Multi-beam multi-wavelength semiconductor lasers. *Appl. Phys. Lett.* **95,** 161108 (2009).
32. Stutzman, W. L. & Thiele, G. A. *Antenna Theory and Design* (John Wiley, 1981).
33. Wang, B., Liu, L. & He, S. Propagation loss of terahertz surface plasmon polaritons on a periodically structured Ag surface. *J. Appl. Phys.* **104,** 103531 (2008).
34. Gaidis, M. C. *et al.* A 2.5-THz receiver front end for spaceborne applications. *IEEE Trans. Microw. Theory Tech.* **48,** 733–739 (2000).
35. Siegel, P. H. & Dengler, R. J. The dielectric-filled parabola: A new millimetre/submillimetre wavelength receiver/transmitter front end. *IEEE Trans. Antennas Propag.* **39,** 40–47 (1991).
36. Belkin, M. A. *et al. Int. Workshop on Optical Terahertz Science and Technology* Talk TuC5, Santa Barbara (2009).
37. Adam, A. J. L. *et al.* Beam patterns of terahertz quantum cascade lasers with subwavelength cavity dimensions. *Appl. Phys. Lett.* **88,** 151105 (2006).
38. Orlova, E. E. *et al.* Antenna model for wire lasers. *Phys. Rev. Lett.* **96,** 173904 (2006).
39. Fan, J. A. *et al.* Wide-ridge metal–metal terahertz quantum cascade lasers with high-order lateral mode suppression. *Appl. Phys. Lett.* **92,** 031106 (2008).
40. Huggard, P. G. *et al.* Drude conductivity of highly doped GaAs at terahertz frequencies. *J. Appl. Phys.* **87,** 2382–2385 (2000).
41. Walukiewicz, W., Lagowski, L., Jastrzebski, L., Lichtensteiger, M. & Gatos, H. C. Electron mobility and free-carrier absorption in GaAs: Determination of the compensation ratio. *J. Appl. Phys.* **50,** 899–908 (1979).
42. Adachi, S. *GaAs and Related Materials: Bulk Semiconducting and Superlattice Properties* (World Scientific Publishing Company, 1994).

Acknowledgements

We gratefully acknowledge constructive and helpful discussions with R. Blanchard, C. Pflügl, L. Diehl and A. Belyanin. M.A.K. is supported by the National Science Foundation through a Graduate Research Fellowship. We would like to thank N. Antoniou for assistance in FIB milling. We acknowledge support from AFOSR under contract No. FA9550-09-0505-DOD and the EPSRC (UK). The authors acknowledge the Center for Nanoscale Systems (CNS) at Harvard University. Harvard CNS is a member of the National Nanotechnology Infrastructure Network (NNIN). The computations in this Letter were run on the Odyssey cluster supported by the Harvard Faculty of Arts and Sciences (FAS) Sciences Division Research Computing Group.

Author contributions

N.Y. designed the devices, in collaboration with J.A.F., and, with Q.J.W., fabricated them and carried out the experiments. M.A.K. participated in the device simulation and in the data analysis. S.P.K. and L.L. grew QCL material using molecular beam epitaxy. N.Y. and F.C. wrote the paper. F.C., A.G.D. and E.H.L. supervised the project.

Additional information

The authors declare no competing financial interests. Supplementary information accompanies this paper on www.nature.com/naturematerials. Reprints and permissions information is available online at http://npg.nature.com/reprintsandpermissions. Correspondence and requests for materials should be addressed to N.Y. or F.C.